Formation and Transient Photovoltaic Properties of ZnO/Si Isotype Heterojunctions by Magnetron Sputtering

V. Melnik, B. Romanyuk, V. Kladko, V. Popov, O. Gudymenko, O. Liubchenko, T. Sabov, O. Oberemok, O. Dubikovskyi, JU. Gomeniuk, O. Kosulya, V. Shmid, A. Podolian, A. Nadtochiy, and O. Korotchenkov

1 Introduction

The integration of thin films with Si technology implies serious limitations of the minimum thickness of the film, allowing to create an isotype heterojunction with high quality. This is a particularly competitive task as numerous thermal treatment steps are usually involved. One of the most important problems in this respect is the need to avoid the formation of large defect concentrations at the film/substrate boundary. It is known that zinc oxide exhibits unique properties, which make it interesting for study and numerous applications [1].

V. Melnik · B. Romanyuk (✉) · V. Kladko · V. Popov · O. Gudymenko · O. Liubchenko · T. Sabov · O. Oberemok · O. Dubikovskyi · JU. Gomeniuk · O. Kosulya
Lashkaryov Institute of Semiconductor Physics, Prospect Nauki, 41, Kiev 03028, Ukraine
e-mail: romb@isp.kiev.ua

V. Melnik
e-mail: romb@isp.kiev.ua

V. Kladko
e-mail: kladko@isp.kiev.ua

V. Popov
e-mail: romb@isp.kiev.ua

O. Gudymenko
e-mail: gudymen@ukr.net

O. Liubchenko
e-mail: lubchenco.a@gmail.com

T. Sabov
e-mail: tsabov92@gmail.com

O. Oberemok
e-mail: ober@isp.kiev.ua

© Springer Nature Switzerland AG 2021

O. Fesenko and L. Yatsenko (eds.), *Nanomaterials and Nanocomposites, Nanostructure Surfaces, and Their Applications*, Springer Proceedings in Physics 246, https://doi.org/10.1007/978-3-030-51905-6_24

One promising type of ZnO-based structures suitable for photovoltaic applications employs undoped ZnO layers grown on Si wafers [2]. Zinc oxide is also a piezoelectric and optical waveguide material, which was used in sensor and ultraviolet (UV) detector, light emitting diode (LED), surface acoustic wave (SAW), and solar cell technologies, as well as transparent electrodes, particularly, carrier-selective contacts with wide band gaps for Si heterojunction solar cells [3–9]. Zinc oxide was also extensively explored for using in transparent thin film transistors (TFTs) [10–12]. High optical transparency in the visible range and low resistivity make ZnO an important material for its using as heat mirrors in stoves, conducting coatings in aircraft glasses to avoid surface icing [13].

The native defects in ZnO, oxygen vacancies V_O and zinc interstitials Zn_i, form donor levels in the forbidden gap, so that zinc oxide is naturally an *n*-type semiconductor [14]. The Si/ZnO heterojunction is also widely employed. The presence of SiO_x native oxide and defects at the interface affects the charge carrier generation and recombination and drastically changes the electrical and photoelectric properties of the heterojunction.

Physical properties of ZnO depend on growth method, impurities, temperature, and other factors, which in turn are important for the effective performance of practical devices. One important prerequisite for the LED applications is the ability to achieve *n* and *p* types of electrical conduction in ZnO [15]. This allowed to fabricate and realize *p*-*n* junction on ZnO and observe electroluminescence in the junction [16, 17]. However, as the acceptor impurities are hardly dissolved, it is still quite difficult to produce *p*-type ZnO [18–20]. Moreover, because of a strong polarization field, the quantum efficiency of ZnO-based LEDs is reduced [21]. It was shown that growing nonpolar films, such as GaN-based layers, can improve the efficiency [22].

Nickel oxide offers an interesting alternative for fabricating ZnO-based heterojunctions, since it is also a wide direct bandgap semiconductor ($E_g = 3.7$ eV) and

---

O. Dubikovskyi
e-mail: dubikovsky_o@ukr.net

JU. Gomeniuk
e-mail: yurigom@lab15.kiev.ua

O. Kosulya
e-mail: alexandr250990@gmail.com

V. Shmid (✉) · A. Podolian · A. Nadtochiy · O. Korotchenkov
Faculty of Physics, Taras Shevchenko Kyiv National University, Volodymyrska 64/13, Kiev
01601, Ukraine
e-mail: shmdvi@gmail.com

A. Podolian
e-mail: summer.podolian@gmail.com

A. Nadtochiy
e-mail: namobem@gmail.com

O. Korotchenkov
e-mail: olegk@univ.kiev.ua

can much simpler be obtained with a *p*-type conductivity [23, 24]. Consequently, *p*-*n* junctions utilizing NiO/ZnO and MgZnO/NiO were successfully fabricated [25–27]. In this respect, metal oxide semiconductor nanocomposite heterojunctions, which combined *n*-type zinc oxide and *p*-type nickel oxide, offered an interesting approach for enlarging the free charge separation lengths increasing their lifetimes [28–34].

Different low-dimensional structures with ZnO, e.g., thin films, nanotubes, nanowires, nanofibers, were fabricated using various deposition techniques, such as MBE, CVD, sol–gel method [35, 36]. Microwaves and sonochemical synthesis were also used [37–40].

Using magnetron sputtering technique, ZnO-on-*p*-Si LEDs were obtained [41]. It was reported in this work that the electroluminescence behavior of the ZnO/Si depends sensitively on the growth conditions. Morphology aspects in thin films of ZnO synthesized with magnetron sputtering method were recently addressed by Nagabharana et al. [42], and a crucial role of the deposition rate in the substrate-ZnO interface bonding was demonstrated.

As reported by Wang et al., changing the deposition temperature of wurtzite ZnO FAZO films, co-doped with fluorine and aluminum, modified the film surface morphology such that “pyramid” and “crater” shapes were observed [43]. These transformations were detected by combining different techniques, e.g., XRD, SEM, AFM, XPS, and optical spectroscopy.

When doping ZnO with Mg, Al, and Ga (AGMZO), the properties of the films, such as structure, morphology, resistivity, and optical transmittance, were found to depend upon the Mg content, as reported by Liu and Zhu [44].

Kim et al. studied ZnO films integrated in the ITO cathodes as transparent buffer layers in inverted polymer solar cells (IPSCs) [45]. Comparing magnetron sputtering and solution-based growth techniques, the authors demonstrated that the power conversion efficiency was much lower in the former growth method. Meanwhile, it exhibited improved performance of ZnO buffers due to the formation of a suitable heterojunction structure

Photoelectrical properties of Cr-doped magnetron-sputtered ZnO layers were studied by Fareed et al. [46]. It was shown that the barrier height in ZnO/Pt Schottky diodes was lowered due to such a doping of ZnO. Moreover, the ideality factor of the diode was made better. Furthermore, the doping induced the diode responsivity in the visible region, although an undoped ZnO film in the photodiode did not show appropriate response. This effect was attributed to the reduction in E_g due to Cr doping.

Frequently, ZnO is doped by the IIIA group elements to obtain a layer with modified properties. Aluminum is the most suitable for this purpose because Al dopant atoms offer an enhanced concentration of free electrons, which increases the electrical conductivity [47]. Besides, adding aluminum into ZnO (AZO films) changes E_g. ZnO:Al/Si heterojunctions have a higher switching speed and lower temperature budget in comparison with typical silicon *p*-*n* or *p*-*i*-*n* junctions. The heterojunction quality depends on the number and type of defects on the interface and in the thin film. Ion implantation with the next temperature treatments allows to change the point defect concentration in ZnO film and obtains the ZnO/Si structures with desired properties.

Here, the charge transport properties related to the different magnetron-sputtered ZnO and NiO thin film and interface morphologies, current-voltage characteristics, and surface photovoltage will be discussed and favorable deposition conditions will be concluded.

Different AZO films with thicknesses varying from 10 to 140 nm were prepared on Si substrates by DC reactive magnetron sputtering. Some of them were modified by using Ar^+ ion implantation (50 and 100 keV). The samples were annealed by rapid thermal and furnace annealing at temperatures ranging from 450 to 750 °C.

The resulting films were studied using XRD, SIMS, SEM, as well as surface photovoltage (SPV) decays. The diode structures were manufactured for investigation of current-voltage (*I*–*V*) and capacitance-voltage (*C*–*V*) characteristics.

2 Formation of ZnO/Si Isotype Heterojunction at Room Temperature and Its Structural and Morphological Properties

Typical ZnO fingerprints with the diffraction lines from (100), (002), and (101) planes are observed in the XRD spectra of AZO grown on Si (see Fig. 1). It is seen that, at film thicknesses smaller than 67 nm, only one peak (002) is seen in the XRD spectra. The (002) peak gains in intensity upon enhancement of the AZO film thickness from 11 to 120 nm. This is indicative of the fact that ZnO columns appear having crystallographic c-axis normal to the substrate surface. Moreover, the (002) peak position shifts to higher diffraction angles for the film thicknesses of 11 and 22 nm, which can be attributed to decreasing the film density with increasing its thickness.

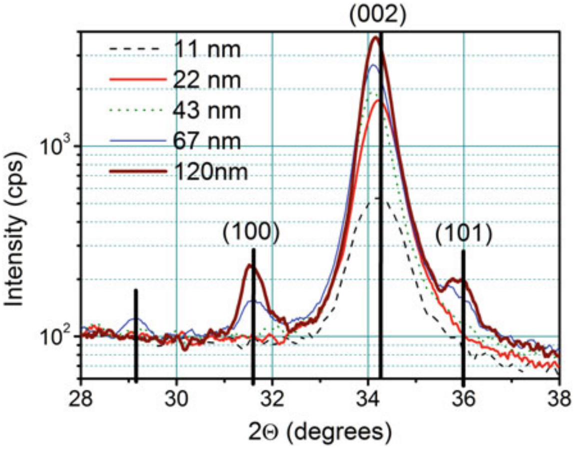

Fig. 1 XRD patterns of different ZnO films grown on Si

Upon increasing the thickness to about 67 nm, the three ZnO fingerprints could be clearly resolved on a semi-log scale of the XRD spectrum. This may be due to the weakening of the influence of the substrate, which thus changes the internal structure of the films. At the film thicknesses of 120 nm, the (101) and (100) peaks gain in intensity.

The above effect of the film loosening with increasing the film thickness is furthermore illustrated by the AFM data shown in Fig. 2. A less tight stacking of the columns in the film, accompanied by an enhanced nanograin density and size, is observed. Indeed, at the film thickness of 11 nm, the surface is smooth and matches with the Si substrate surface relief, as observed in image a in Fig. 2. This trend toward nanograin formation with the size from 10 to 15 nm is clearly visible as bright white spots distributed across the image a. The size and the density of these features gradually increase with increasing the film thickness (b and c in Fig. 2) until the tight consolidated layer is formed when it reaches a critical size greater than ≈65 nm (d and e in Fig. 2). In the latter case, the grain diameter reaches the value from 10 to 60 nm. It has been found that a bimodal grain size distribution peaked at 20 and 50 nm is observed in the 120-nm film.

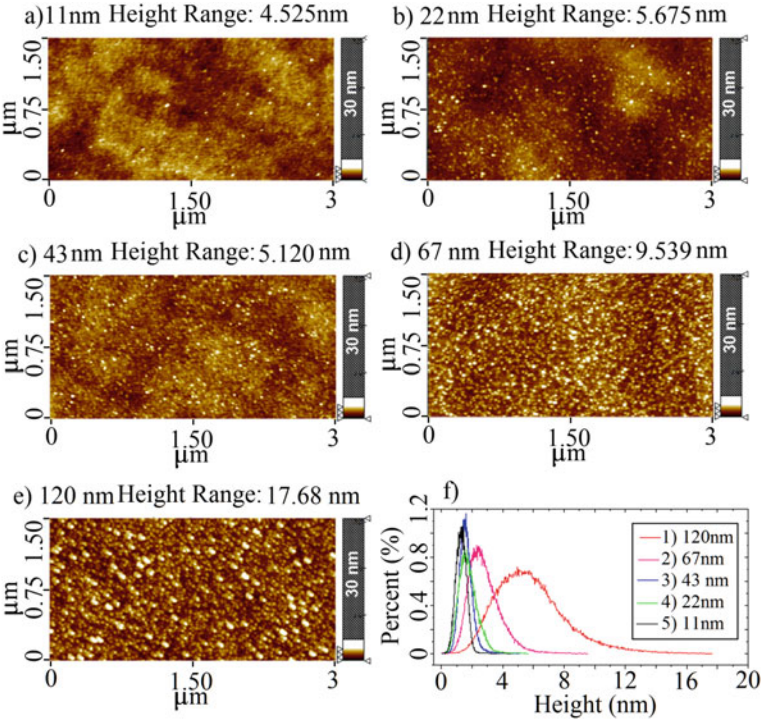

Fig. 2 Typical AFM surface profiles of ZnO films having thicknesses of 11, 22, 43, 67, and 120 nm (**a**–**e**) deposited onto the Si substrate. Height distribution histograms of the film surfaces are shown in (**f**)

Fig. 3 XRD pattern of a 65.8-nm thick ZnO film

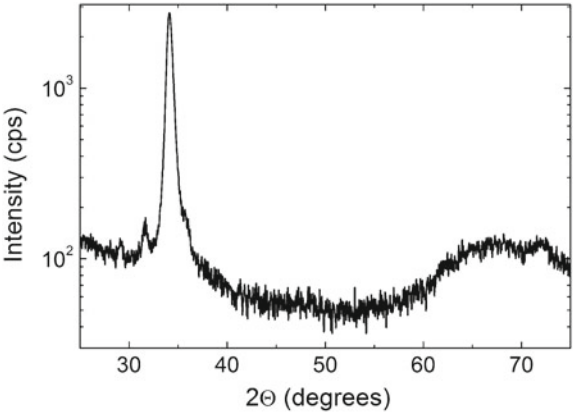

Of further significance is the fact that the ZnO films with thicknesses less than 50 nm are textured. At greater thicknesses, a polycrystalline structure of hexagonal modification is formed (Fig. 3). This may originate from the large difference in the lattice parameters of Si and ZnO, which leads to an inhomogeneous growth of the ZnO film at small thicknesses.

From XRR studies, thickness, density, and root mean squared (rms) roughness of deposited films are determined. This procedure yields the values given in Table 1. It is found that the roughness of the Si/ZnO interface does not significantly change upon increasing the film thickness, for the thicknesses less than ≈70 nm, as evidenced by the data shown in Fig. 4. In turn, the surface roughness exhibits a noticeable increase within the thickness range.

Further insight into the processes associated with the growth of ZnO:Al (AZO) films can be obtained by analyzing the SEM images shown in Fig. 5. It is seen that the surface relief has an irregular grainy structure character, whereas the inner region of the film forms a consolidated layer, which can be due to Al inclusions in ZnO.

Mass spectrometric studies given in Fig. 6 shows an ultra-thin SiO_2 oxide film layer having the thickness of about 2 nm that is formed on the boundary of the phase separation, implying that AZO/SiO_2/Si interface is formed in the samples. This is a prerequisite for considering tunneling through the oxide film (tunnel current) as the

Table 1 Parameters of ZnO-on-Si films discussed in this work

Sample No.	Film thickness (nm)	Film density (g/cm^3)	ZnO/Si interface rms roughness measured by XRR (nm)	ZnO surface rms roughness measured by XRR (nm)
1	10.2	5.9	0.4	0.54
2	20.8	5.62	0.34	0.52
3	41.6	5.59	0.02	0.51
4	65.8	5.60	0.05	0.6

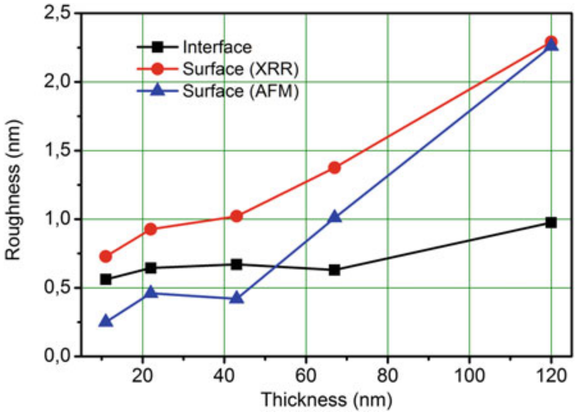

Fig. 4 Surface and interface roughness of different ZnO-on-Si films inferred from the XRR and AFM data

dominant free electron transport mechanism in these structures. It is also shown in Fig. 6 that the Al impurity is homogeneously distributed over the thickness of the film.

It should be noted that some features of the distribution of SiO_2^- ions is shown in Fig. 6, namely the presence of two maxima near the boundary of phase separation. This is due to the peculiarities of the origin and growth of the ZnO film at the initial stages of magnetron sputtering. In order to clarify this issue and find out the role played by the above nanograins formed at small film thicknesses, processes of film recrystallization after their amorphization with argon ions and annealing have been studied. Some results are exemplified in Fig. 7. Comparing these data for an as-grown (ZnO) and ion implanted (ZnO + I) sample shows that the Ar^+ ion implantation causes the compressive strain in a crystal orientation perpendicular to the ZnO/Si interface (along the c-axis). Increasing the implantation dose and ion energy increases the strain in the film. It has also been verified that the thickness of the films decreases somewhat upon implantation due to decreased inter-grain spacing while their porosity concomitantly increases.

Adding Al during the growth tightens the film, enhances the electrical conductivity and varies the bandgap of ZnO. The thickness of an intermediate SiO_x layer developed at the ZnO/Si interface has been found to be nearly independent of the film thickness.

3 Current-Voltage Characteristics

Dark current-voltage characteristics are shown in Fig. 8a. It is seen that diode-like current-voltage $I(V)$ characteristics appear at film thicknesses greater than ≈60 nm. Reducing the film thickness leads to a significant increase in reverse currents and shortened diode. It has been found that ZnO/Si heterostructures are photosensitive under illumination with wavelengths from 400 nm to 2.5 µm, and a typical result is exemplified in Fig. 8b.

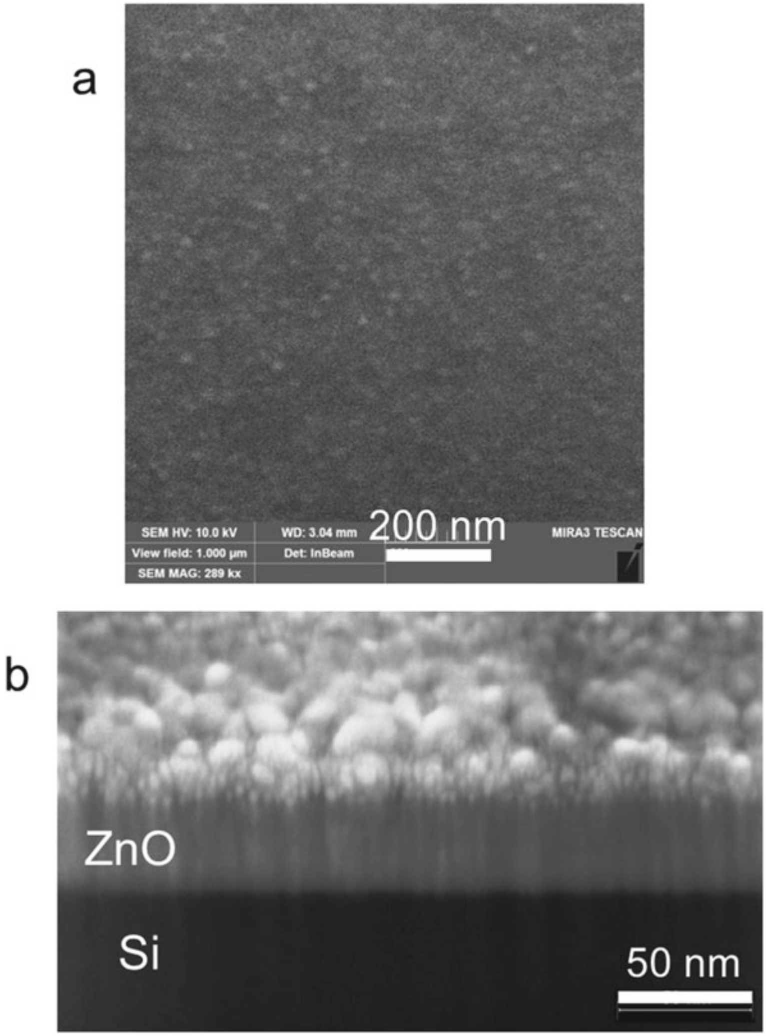

Fig. 5 Surface (**a**) and cross section (**b**) SEM images of a 67-nm thick ZnO film deposited onto the Si substrate

Voltage-capacitance $C(V)$ characteristics taken at frequencies of 1, 10, 100, and 1000 kHz are shown in Fig. 9a. One can see that the barrier capacitance depends upon the signal frequency. The capacitance decreases with increasing the frequency, illustrating the occurrence of interface states that cannot trace the quicker signal change with increasing the frequency.

In this respect, the effect of aluminum segregation at the AZO/SiO_2/Si interface was discussed, e.g., by Bikowski et al. [48] and Jaramillo et al. [11]. This may be due to the domination of either aluminum condensation or zinc re-evaporation at the

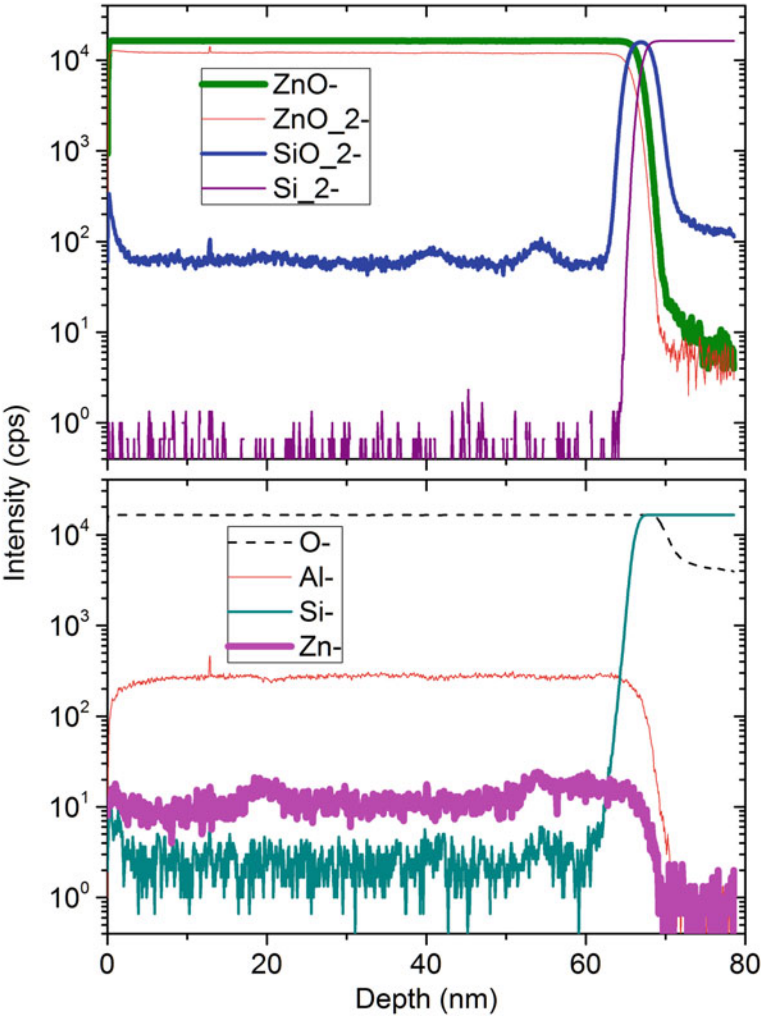

Fig. 6 In-depth elemental distributions in SIMS profiling analysis of a 67-nm thick ZnO film deposited onto the Si substrate

interface at the beginning of the deposition of AZO. As reported by Bikowski et al. [48], the condensation and re-evaporation effects can be related to the vapor pressure during the growth. Moreover, according to Alcock et al. [49], the evaporation rate of Zn is much greater than that of Al. In contrast, metal oxides tend to reside on the surface much stronger than pure metals since the pressure of vapor is considerably smaller in the former case. Furthermore, the formation of aluminum oxide or aluminum-doped zinc oxide is energetically favorable compared to formation of zinc oxide. Therefore, this can explain the domination of the segregated aluminum mentioned above during the deposition at high substrate temperatures.

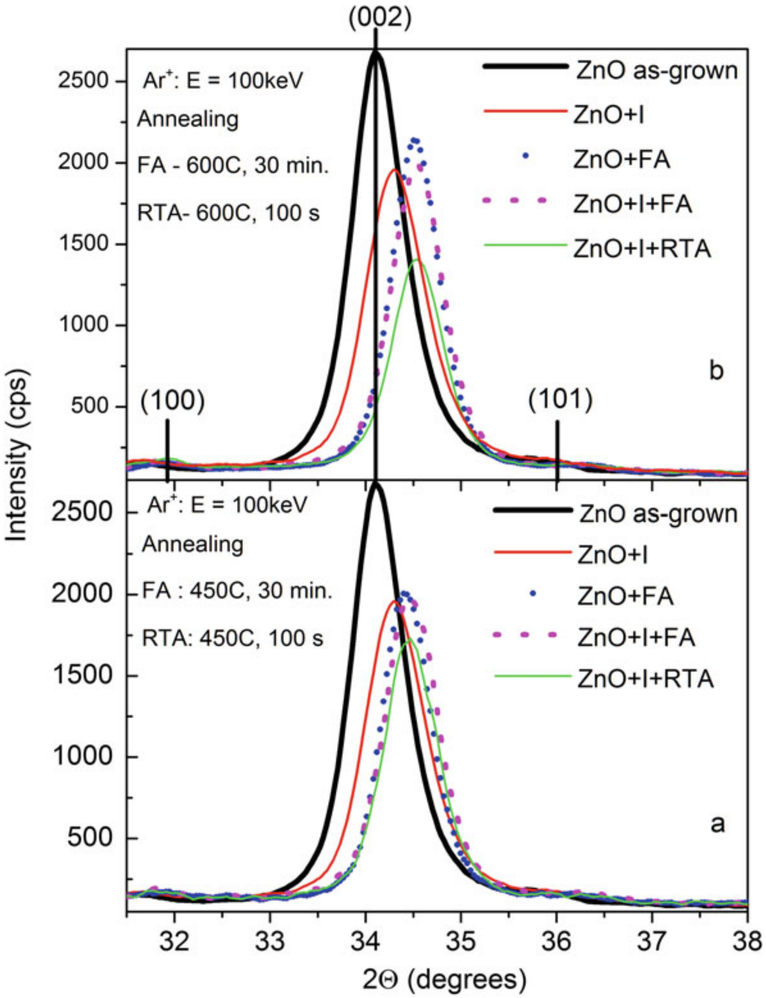

Fig. 7 XRD spectra of ZnO films, as-grown (ZnO as-grown) and processed either upon 450 °C (**a**) or 600 °C (**b**) annealing for 30 min (ZnO + FA) or implanting with 100 keV Ar^+ ions (ZnO + I) followed by annealing at 450 °C (**a**) or 600 °C (**b**) for 100 s (ZnO + I+RTA) or 30 min (ZnO + I + FA)

This in turn suggests that the AZO film is highly doped at the interface. Therefore, the AZO/Si junction is asymmetric with a thicker space charge region in the Si substrate compared with that in the ZnO film. Then the capacitance is simply $C \approx \varepsilon_{\mathrm{Si}}/W$, where $\varepsilon_{\mathrm{Si}}$ is the dielectric constant of Si, and W is the total thickness of the space charge region. At reverse bias, the capacitance depends only weakly on the frequency. In turn, at forward bias, the free electrons in Si are captured at the interface states thus decreasing the capacitance with increasing the frequency.

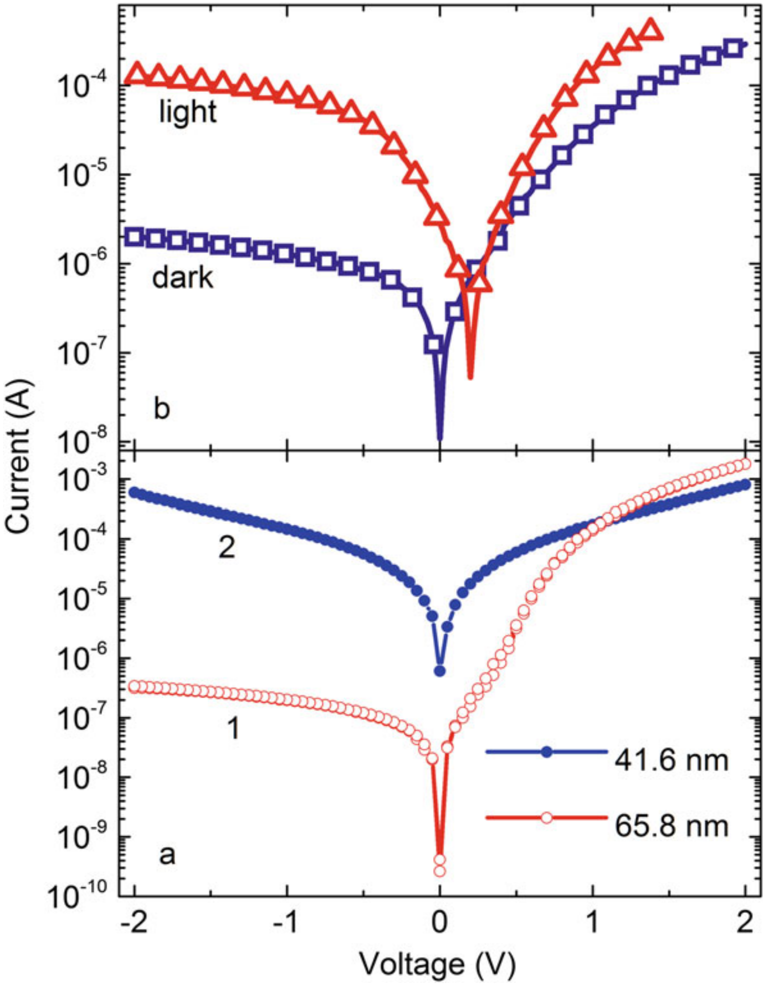

Fig. 8 **a** Dark $I(V)$ curves of ZnO-on-Si films having a thickness of 65.8 nm (1) and 41.6 nm (2). **b** $I(V)$ curves of ITO/ZnO/Si structure in the dark and at an illumination with white light

The appearance of peaks in the $C(V)$ curves shows evidence of tunneling through the interface states and oxide film discussed above. Replotting the data of Fig. 9a in the form of $1/C^2$ versus V in Fig. 9b yields the barrier height V_b of 0.66 eV. It has been observed that V_b depends on the annealing temperature of the implanted structures.

One thus concludes that the distribution of aluminum-rich phases has yet been studied insufficiently in magnetron-sputtered AZO films. In particular, Sieber et al. [50] addressed the microstructural properties of ZnO:Al, illustrating the occurrence of zinc–aluminum–oxygen phases, 10–20 nm beneath the Si substrate. However,

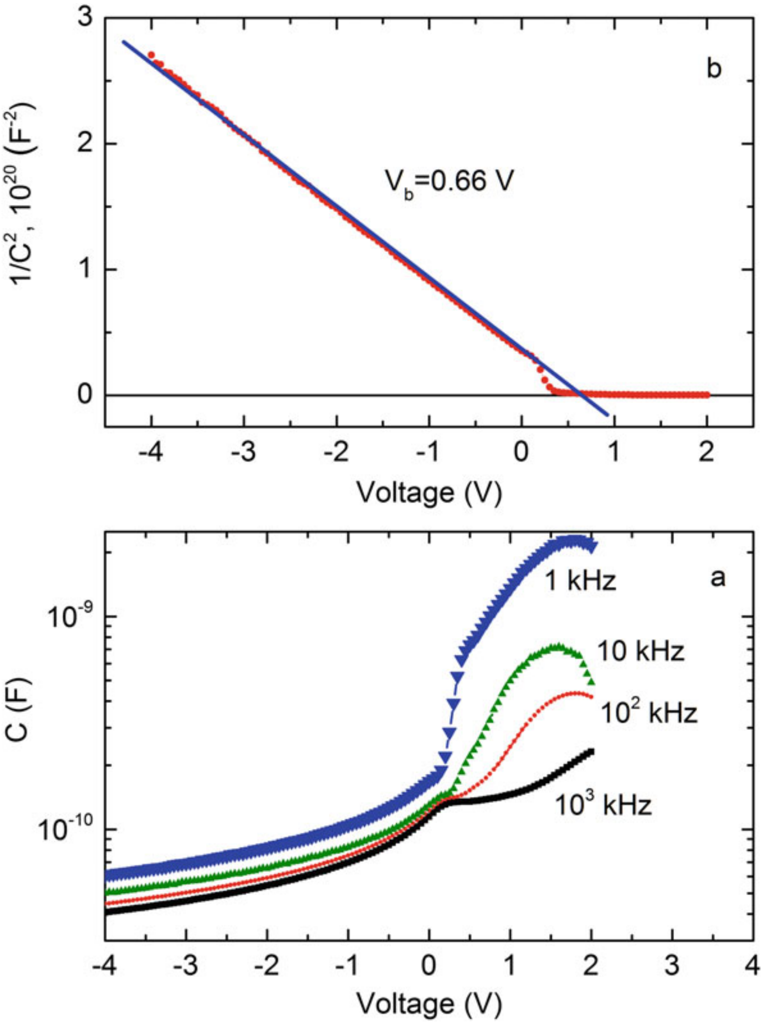

Fig. 9 **a** Voltage-capacitance characteristics of ZnO film with a thickness of 65.8 nm grown on Si (**a**) and determination of the potential barrier value in this ZnO/Si structure (**b**)

the film electrical conductivity remained uncovered in this study. Kinemuchi et al. reported aluminum-rich boundaries in ceramic AZO grains [51].

In the remaining part of this work, we, therefore, present photoelectrical properties of the films, and, particularly, spatially distributed SPV signals, which can shed light on some of the above segregation problems unsolved so far.

4 Transient Surface Photovoltage

Surface photovoltage (SPV) is formed by the separation of nonequilibrium carriers in the near-surface sample region [52]. In particular, the separation exists in the space charge regions that occur on the sample surfaces or at grain boundaries and interfaces. The magnitude and direction of the appropriate band bending in these regions determine the magnitude and sign of the SPV signal formed under light illumination. The band bending itself depends on the concentration and type of defects in surface and interface areas. These concentrations and type also determine the generation and recombination velocity of nonequilibrium free charges.

In our case of ZnO/SiO_2/Si heterostructures, the SPV amplitude and decay times taken after the light is turned off can, in general, be related to varying defect content in ZnO films and in a narrow subsurface region of the Si substrate. The SPV characteristics would therefore depend on the deposition method and thickness of the ZnO layer. Measuring SPV can furthermore be interesting for improving the photovoltaic properties of ZnO/SiO_2/Si and NiO/ZnO/Si heterostructures.

Varying the light wavelength, one can vary the light penetration depth into the semiconductor structure, thus appropriately changing the carrier generation depth spanning the junction regions of the heterostructures. This is particularly true in case of small pulse widths of the illuminating light, when the width remains much smaller than the carrier lifetime. Otherwise, if the light pulse is of the order of or greater than the lifetime of nonequilibrium carriers, then the carriers from a thick subsurface layer comparative with their diffusion length contribute to the SPV signal, even for the strongly absorbed light [53].

Taking the bandgap $E_g = 3.2$–3.3 eV in ZnO [54] and $E_g = 1.12$ eV in the Si substrate [55] one gets that exciting light with $\lambda > 375$ nm correspond to E_g of ZnO [54]. Therefore, the SPV signal generated by a visible light is formed only by free carriers excited in the Si substrate. For the light with a wavelength of less than $\approx$375 nm, the signal will come from nonequilibrium carriers generated both in the ZnO film and Si substrate. Strictly speaking, for both excitation conditions, one should take into account the carrier diffusion and drift from the Si substrate into the ZnO film and in the opposite direction.

The SPV data given below were measured in the capacitance arrangement and the measurement technique was described in detail in [56]. SPV decay curves taken in different ZnO-on-Si samples are shown in Fig. 10. The samples are excited by light pulses of 1 μs duration with three different wavelengths $\lambda = 405$ nm, 470 nm, and 860 nm. At these conditions, nonequilibrium charge carriers are generated only in the Si substrate at depths of $1/\alpha \approx 98$ nm, 312 nm, and 21 μm, respectively, where α is the light absorption coefficient in Si for the above three excitation wavelengths [55]. Negative SPV signals were experimentally detected in the circuit schematics used and, for convenience, they are shown in Fig. 10 as well as in the text that follows, the SPV decay curves are inverted.

It is shown in Fig. 10 that regardless of the wavelength of the exciting light, the SPV decay rate decreases monotonically with increasing the ZnO thickness from 11

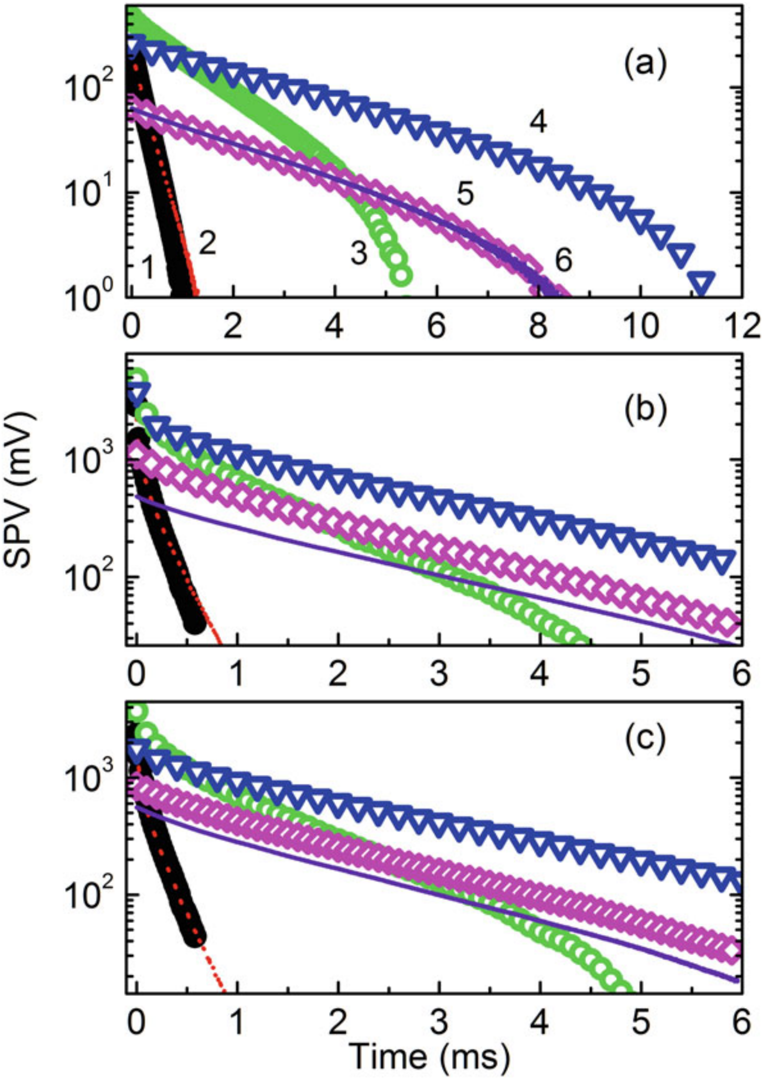

Fig. 10 SPV decay curves in ZnO/Si excited with LED light of wavelengths $\lambda = 405$ nm (**a**), 470 nm (**b**) and 860 nm (**c**). The light pulse width is 1 μs. The thickness of ZnO films is 11 (curve 1), 22 (2), 43 (3), 67 (4), 70 (5), and 120 nm (6)

to 67 nm. When further increasing the thickness to 120 nm, the decay rate of the SPV signal remains nearly unchanged. At the same time, when the thickness increases from 11 to 43 nm, the SPV amplitude value first increases monotonically and then begins to decrease for greater thicknesses (up to 120 nm).

If the same samples are excited by light pulses of 10 ns duration from a nitrogen laser ($\lambda = 337.1$ nm), the decay curves shown in Fig. 11 are observed. Under these

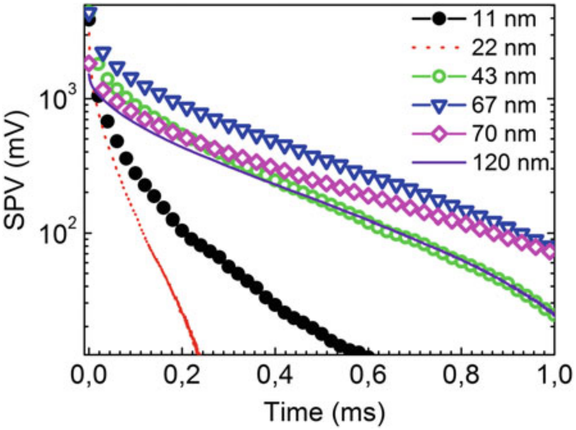

Fig. 11 SPV decay curves in ZnO films with different thicknesses grown on Si excited with N_2 laser light ($\lambda = 337.1$ nm) having pulse width of 10 ns

excitation conditions, nonequilibrium charge carriers are generated both in the ZnO film and Si substrate with a depth of $1/\lambda \approx 9$ nm [55]. It can be found that, in this case, the decay curves are described by a biexponential law. The appropriate time constants of both the first and second components increase with increasing the thickness of ZnO from 11 to 120 nm (see Fig. 12a). In contrast, the magnitude of the SPV signal first increases slightly at film thicknesses varying from 11 to 67 nm and then sharply decreases at the thicknesses greater ≈ 70 nm; see Fig. 12b.

Next, Fig. 13 shows the distributions of the SPV decay time constant τ across the sample surface taken for different thicknesses of the ZnO film. Appropriate distributions of the SPV amplitude are given in Fig. 14. The data of Figs. 13 and 14 are taken when scanning the surfaces of the samples with a narrow light beam of a laser diode with $\lambda = 630$ nm with a spatial resolution of 100 μm. This scanning SPV apparatus has been discussed elsewhere [57].

It is shown in Fig. 13 that the width of the distribution function for τ increases for the thicknesses from 11 to 120 nm. The maximum of the distribution shifts toward greater values of τ. At the same time, the width of the distribution function for the SPV amplitude shown in Fig. 14 first increases in the thickness range from 11 to 43 nm and then decreases very sharply for 67–120 nm thicknesses. In this case, the distribution maximum shifts toward greater values of the SPV amplitude for the thickness range from 11 to 67 nm and then, at greater thicknesses from 70 to 120 nm, shifts to almost 100% of its initial value.

These SPV results can be explained as follows by taking the change of the film morphology with its thickness into consideration. The film microstructure changes significantly with increasing the thickness (see Fig. 2). Thus, the size of nanograins and nanocolumns can vary from about 10 to 60 nm for the film thickness $\leq$67 nm, until the tight consolidated layer is formed in the range from about 65 to 120 nm.

Consistent with these observations, increased SPV amplitude values are detected primarily due to a larger spatial separation of photogenerated carriers in larger grains. Furthermore, the observed broadening of the SPV amplitude distribution can be

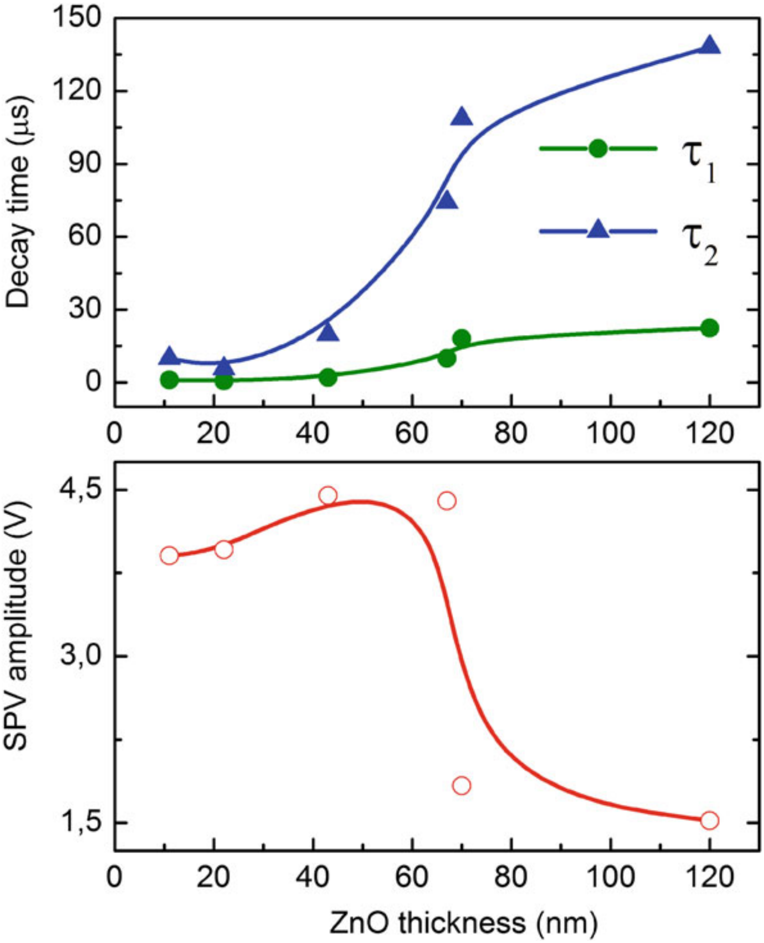

Fig. 12 SPV decay time (**a**) and amplitude (**b**) in ZnO/Si versus the thickness of ZnO films excited with N_2 laser light ($\lambda = 337.1$ nm) having a pulse width of 10 ns

explained by a concomitantly broader dispersion in grain sizes. It appears that in the thickness range from about 65 to 120 nm, when a dense consolidated layer occurs, the SPV amplitude decreases with a narrowing of its distribution function across the sample surface. Moreover, the observed increase in τ, broadening of the distribution of τ, and a shift of the maximum value of this distribution to greater τ are most likely due to the fact that increasing the grain size and grain density affects the composition and concentration of recombination-active defects at grain boundaries. Finally, carrier trapping at deep levels and grain surface or interface states may become dominating over fast carrier recombination processes, which also increases τ.

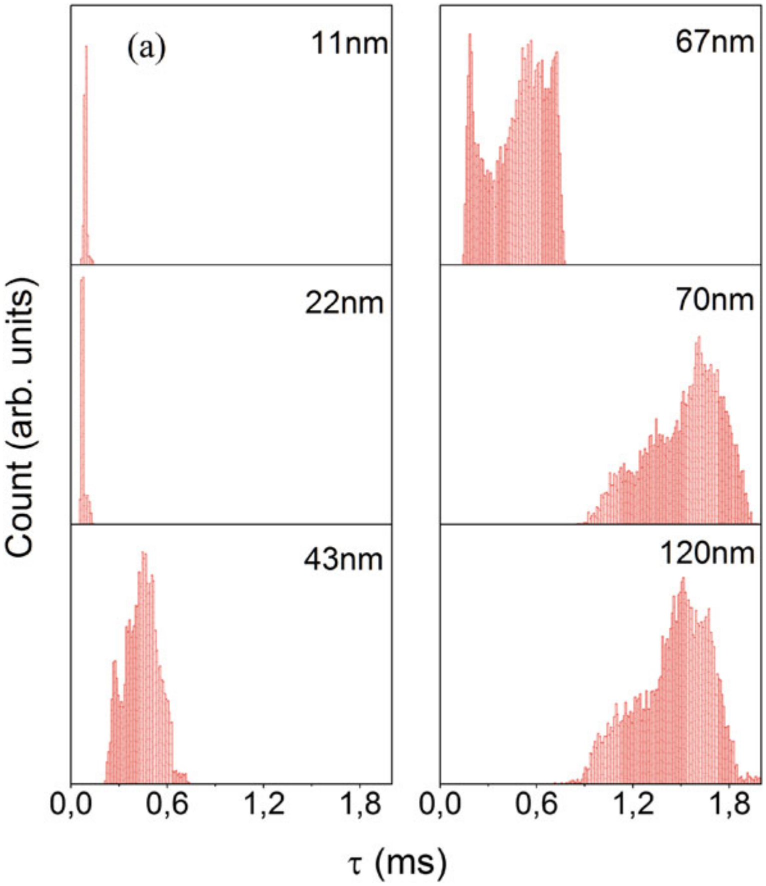

Fig. 13 Probability functions of the surface distribution of τ in ZnO/Si with different thickness of ZnO layer. See measurement details in [57]

For comparison, the SPV attenuation curves were also measured on a sample in which a *p*-NiO film, ≤70 nm thick, was additionally deposited on top of a 120 nm thick ZnO film. In this structure, the NiO/ZnO interface forms a *p*-*n* junction, which in turn should enlarge the SPV magnitude due to increased number of photoexcited carriers separated by the *p*-*n* junction field.

In Fig. 15, we show SPV decay curves for samples with a 120 nm ZnO film without (curve 1) and with an additional *p*-NiO layer (curve 2). These samples are excited by light pulses of 1 μs duration with wavelength of 405 nm.

Most significantly, the deposition of an additional *p*-NiO layer increases the SPV magnitude by about 3 times, while the SPV decay time also increases significantly. Again, this increase in the SPV amplitude comes from the *p*-NiO/*n*-ZnO junction. The shortened SPV decay is apparently due to enhanced recombination rate

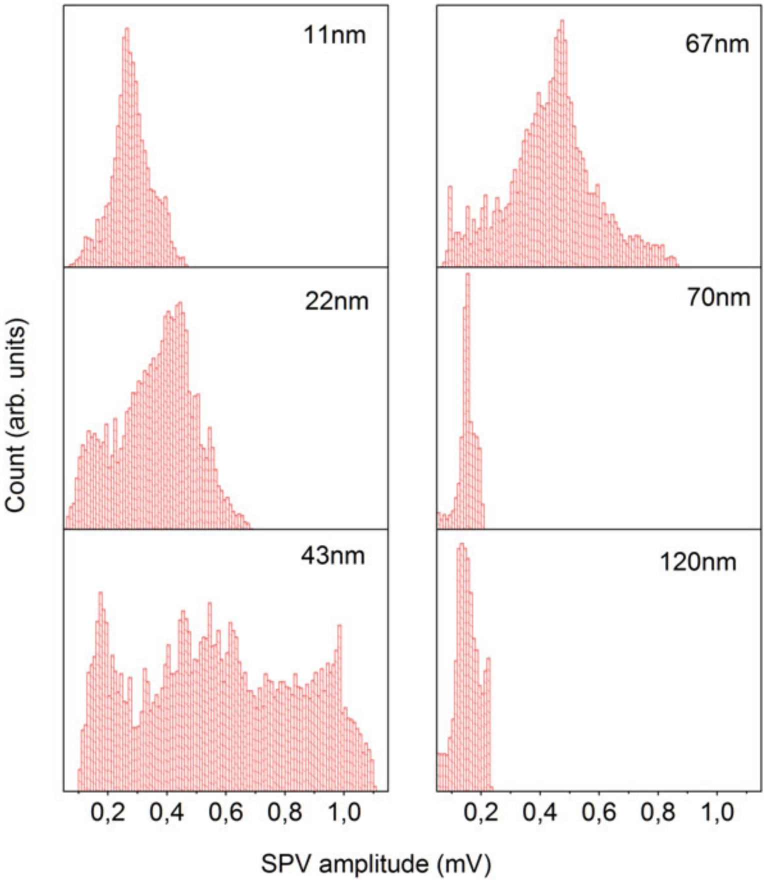

Fig. 14 Probability functions of the surface distribution of the SPV amplitude in ZnO/Si with different thickness of ZnO layer

Fig. 15 SPV decay curves in ZnO/Si (1) and *p*-NiO/*n*-ZnO (2) excited with $\lambda = 405$ nm light having pulse width of 1 μs. The thickness of ZnO films is 120 nm in both cases, the thickness of NiO is about 70 nm

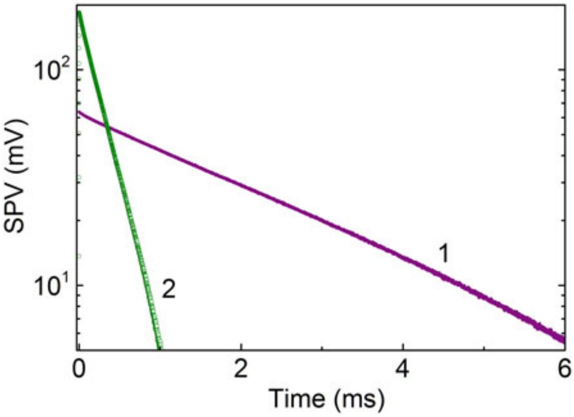

of photogenerated carriers at the additional recombination centers formed at this interface.

5 Conclusions

In summary, the structural and electro-physical characteristics of ZnO/Si heterostructures formed by the magnetron film deposition from aluminum-doped ZnO target are addressed. The film recrystallization and microcrystal structure restoration are observed. It is found that the ZnO/Si barrier is about 0.66 eV and depends on the annealing temperature of the implanted structures. Diode structures with a transparent electrode (ITO/ZnO/Si/Al) have photosensitivity in the wide spectral region of 0.4–2.5 μm. The photosensitivity mechanisms in different spectral bands require further refinement.

The deposited ZnO films with thicknesses of less than $\approx$70 nm have roughly three times greater photovoltage magnitude compared with that having greater thicknesses, and this coincide with the microstructural evolution of the film. The SPV decays slow down accordingly exhibiting decay times of the order 10 μs at the small film thicknesses and 100 μs at the ones exceeding $\approx$70 nm. These results can be interpreted in terms of the recombination and carrier trapping centers in the film and at the ZnO/Si boundary, whose concentration varies with the film thickness.

It is furthermore shown that forming *p*-NiO/*n*-ZnO/Si heterostructure increases the photovoltage magnitude, which is up to several times, and shortens the SPV decays. This can be effectively used in manufacturing rapid photosensitive elements.

References

1. Pearton SJ, Norton DP, Ip K, Heo YW, Steiner T (2005) Recent progress in processing and properties of ZnO. Prog Mater Sci 50(3):293–340
2. Bedia Z, Bedia A, Kherbouche D, Benyoucef B (2013) Electrical properties of ZnO/p-Si heterojunction for solar cell application. Int J Mater Eng 3:59–65
3. Purica M, Budianu E, Rusu E (2000) Heterojunction with ZnO polycrystalline thin films for optoelectronic devices applications. Microelectr Eng 51–52:425–431
4. Zheng ZQ, Yao JD, Wang B, Yang GW (2015) Light-controlling, flexible and transparent ethanol gas sensor based on ZnO nanoparticles for wearable devices. Sci Rep 5:11070
5. Shih CC, Lee WY, Chiu YC, Hsu HW, Chang HC, Liu CL, Chen WC (2016) Transistor memory devices using nano-floating gate of polymer/ZnO nanocomposites. Sci Rep 6:20129
6. Umit O, Daniel H, Hadis M (2010) ZnO devices and applications: a review of current status and future prospects. Proc IEEE 98(7):1255–1268
7. Battaglia C, de Nicolás SM, Wolf SD, Yin X, Zheng M, Ballif C, Javey A (2014) Silicon heterojunction solar cell with passivated hole selective MoO_x contact. Appl Phys Lett 104:113902
8. Islam R, Shine G, Saraswat KC (2014) Schottky barrier height reduction for holes by Fermi level depinning using metal/nickel oxide/silicon contacts. Appl Phys Lett 105:182103

9. Cole JJ, Wang X, Knuesel HO, Jacobs RJ (2008) Integration of ZnO microcrystals with tailored dimensions forming light emitting diodes and UV photovoltaic cells. Nano Lett 8:1477–1481
10. Faber H, Klaumünzer M, Voigt M, Galli D, Vieweg BF, Peukert W, Spiecker E, Halik M (2011) Morphological impact of zinc oxide layers on the device performance in thin-film transistors. Nanoscale 3:897–899
11. Jaramillo R, Youssef A, Akey A, Schoofs F, Ramanathan S, Buonassisi T (2016) Using atom-probe tomography to understand ZnO:Al/SiO_2/Si Schottky diodes. Phys Rev Appl 6:034016
12. Hubya N, Ferrari S, Guziewicz E, Godlewski M, Osinniy V (2008) Electrical behavior of zinc oxide layers grown by low temperature atomic layer deposition. Appl Phys Lett 92:023502
13. Wisz G, Virt I, Sagan P, Potera P, Yavorskyi R (2017) Structural, optical and electrical properties of zinc oxide layers produced by pulsed laser deposition method. Nanoscale Res Lett 12:253
14. Janotti A, Van de Walle CG (2009) Fundamentals of zinc oxide as a semiconductor. Rep Prog Phys 72:126501
15. Ozgür U, Alivov YI, Liu C, Teke A, Reshchikov MA, Doğan S, Avrutin V, Cho SJ, Morkoç HA (2005) Comprehensive review of ZnO materials and devices. J Appl Phys 98:041301
16. Chu S, Lim JH, Mandalapu LJ, Yang Z, Li L, Liu JL (2008) Sb-doped p-ZnO/Ga-doped n-ZnO homojunction ultraviolet light emitting diodes. Appl Phys Lett 92:152103
17. Xu WZ, Ye ZZ, Zeng YJ, Zhu LP, Zhao BH, Jiang L, Lu JG, He HP (2006) ZnO light-emitting diode grown by plasma-assisted metal organic chemical vapor deposition. Appl Phys Lett 88:173506
18. Liu W, Gu SL, Ye JD, Zhu SM, Liu SM, Zhou X, Zhang R, Shi Y (2006) Blue-yellow ZnO homostructural light-emitting diode realized by metalorganic chemical vapor deposition technique. Appl Phys Lett 88:092101
19. Xiao ZY, Liu YC, Mu R, Zhao DX, Zhang JY (2008) Stability of p-type conductivity in nitrogen-doped ZnO thin film. Appl Phys Lett 92:052106
20. Ma MJ, Lu B, Zhou TT, Ye ZZ, Lu JG, Pan XH (2013) Orientation dependent band alignment for p-NiO/n-ZnO heterojunctions. J Appl Phys 113:163704
21. Waltereit P, Brandt O, Trampert A, Grahn HT, Menniger J, Ramsteiner M, Reiche M, Ploog KH (2000) Nitride semiconductors free of electrostatic fields for efficient white light-emitting diodes. Nature 406:865
22. Pant P, Budai JD, Aggarwal R, Narayan R, Narayan J (2009) Thin film epitaxy and structure property correlations for non-polar ZnO films. Acta Mater 57:4426
23. Zhang Z, Zhao Y, Zhu M (2006) NiO films consisting of vertically aligned cone-shaped NiO rods. Appl Phys Lett 88:033101
24. Ohta H, Hirano M, Nakahara K, Maruta H, Tanabe T, Kamiya M, Kamiya T, Hosono H (2003) Fabrication and photoresponse of a pn-heterojunction diode composed of transparent oxide semiconductors, p-NiO and n-ZnO. Appl Phys Lett 83:1029
25. Long H, Fang GJ, Huang HH, Mo XM, Xia W, Dong BZ (2009) Ultraviolet electroluminescence from ZnO/NiO-based heterojunction light-emitting diodes. Appl Phys Lett 95:013509
26. Wang JY, Lee CY, Chen YT, Chen CT, Chen YL, Lin CF, Chen YF (2009) Double side electroluminescence from p-NiO/n-ZnO nanowire heterojunctions. Appl Phys Lett 95:131117
27. Deng R, Yao B, Li YF, Zhao YM, Li BH (2009) X-ray photoelectron spectroscopy measurement of n-ZnO/p-NiO heterostructure valence-band offset. Appl Phys Lett 94:022108
28. Xi YY, Hsu YF, Djurisic AB, Ng AMC, Chan WK, Tam HL, Cheah KW (2008) NiO/ZnO light emitting diodes by solution-based growth. Appl Phys Lett 92:113505
29. Wang H, Fang G, Huang H, Mo X, Xia W, Dong B, Meng X, Zhao X (2011) Ultraviolet electroluminescence properties of the p-NiO/n-GaN-based heterojunction diodes. Semicond Sci Technol 26:125015
30. Abbasi MA, Ibupoto ZH, Khan A, Nur O, Willander M (2013) Fabrication of UV photo-detector based on coral reef like p-NiO/n-ZnO nanocomposite structures. Mater Lett 108:149–152
31. Hasan MR, Xie T, Barron SC, Liu G, Nguyen NV, Motayed A, Rao MV, Debnath R (2015) Self-powered p-NiO/n-ZnO heterojunction ultraviolet photodetectors fabricated on plastic substrates. APL Mater 3:106101

32. Baraik K, Singh SD, Kumar Y, Ajimsha RS, Misra P, Jha SN, Ganguli T (2017) Epitaxial growth and band alignment properties of NiO/GaN heterojunction for light emitting diode applications. Appl Phys Lett 110:191603
33. Jumaand AO, Matibini A (2017) Synthesis and structural analysis of ZnO-NiO mixed oxide nanocomposite prepared by homogeneous precipitation. Ceram Int 43:15424–15430
34. Majeed AMA, Nusseif AD, Hameed NS (2019) Investigations of ZnO-NiO/PSi heterojunction for solar cell application. AIP Conf Proc 2144:030015
35. Li X, Shen R, Zhang B, Dong X, Chen B, Zhong H, Cheng L, Sun J, Du G (2011) Nitrogen doped ZnO thin films prepared by photo-assisted metalorganic chemical vapor deposition. J Nanosci Nanotechnol 11:9741–9744
36. Roshchina NM, Smertenko PS, Stepanov VG, Zavyalova LV, Lytvyn OS (2013) Some properties of thin film structures on the base of ZnO obtained by MOCVD method. Solid State Phenom 256:228–236
37. Chatel G, Macfarlane DR (2014) Ionic liquids and ultrasound in combination: synergies and challenges. Chem Soc Rev 43:8132–8149
38. Hosni M, Farhat S, Schoenstein F, Karmous F, Jouini N, Viana B, Mgaidi A (2014) Ultrasound assisted synthesis of nanocrystalline zinc oxide: experiments and modeling. J Alloy Compd 615:S472–S475
39. Zakirov MI, Korotchenkov OA (2017) Carrier recombination in sonochemically synthesized ZnO powders. Mater Sci Pol 35:211–216
40. Zakirov MI, Kuryliuk VV, Korotchenkov OA (2016) Optical properties of ZnO fabricated by hydrothermal and sonochemical synthesis. J Phys Conf Ser 741:012028
41. Ji PF, Li Y, Zhou FQ, Song YL, Huang HC (2019) Fabrication and electroluminescence of sheet-like ZnO/Si light-emitting diodes by radio frequency magnetron sputtering method. Mater Lett. http://www.doi.org/10.1016/j.matlet.2019.127028 (in Press)
42. Nagabharana RM, Kiran N, Guha P, Sundaravel B, Bhatta UM (2019) Structural characterization of magnetron sputtered ZnO thin films on Si(100) using RBS, scanning and high resolution transmission electron microscopy methods. Surf Interfaces 15:239–243
43. Wang Y, Song J, Zhang J, Zheng G, Duan X, Xie X, Han B, Meng X, Yang F, Wang G, Zhao Y, Li J (2019) Effect of substrate temperature on F and Al co-doped ZnO films deposited by radio frequency magnetron sputtering. Sol Energy 194:471–477
44. Liu Y, Zhu S (2019) Preparation and characterization of Mg, Al and Ga co-doped ZnO transparent conductive films deposited by magnetron sputtering. Results Phys 14:102514
45. Kim H-K, Chung K-B, Kal J (2019) Comparison of ZnO buffer layers prepared by spin coating or RF magnetron sputtering for application in inverted organic solar cells. J Alloys Compd 778:487–495
46. Fareed S, Jamil A, Tiwari N, Rafiq MA (2019) Influence of Cr doping on Schottky barrier height and visible light detection of ZnO thin films deposited by magnetron sputtering. Micro Nano Eng 2:48–52
47. Ellmer K, Bikowski A (2016) Intrinsic and extrinsic doping of ZnO and ZnO alloys. J Phys D Appl Phys 49:413002
48. Bikowski A, Rengachari M, Nie M, Wanderka N, Stender P, Schmitz G, Ellmer K (2015) Research update: Inhomogeneous aluminium dopant distribution in magnetron sputtered ZnO: Al thin films and its influence on their electrical properties. APL Mater 3:060701
49. Alcock CB, Itkin VP, Horrigan MK (1984) Vapour pressure equations for the metallic elements: 298–2500K. Can Metall Q 23:309–313
50. Sieber I, Wanderka N, Urban I, Dörfel I, Schierhorn E, Fenske F, Fuhs W (1998) Electron microscopic characterization of reactively sputtered ZnO films with different Al-doping levels. Thin Solid Films 330:108–113
51. Kinemuchi Y, Nakano H, Kaga H, Tanaka S, Uematsu K, Watari K (2011) Microstructural evidence of Hall mobility anisotropy in c-axis textured Al-doped ZnO. J Am Ceram Soc 94:2339–2343
52. Kronik L, Shapira Y (1999) Surface photovoltage phenomena: theory, experiment, and applications. Surf Sci Rep 37:1–206

53. Luke KL, Cheng LJ (1987) Analysis of the interaction of a laser pulse with a silicon wafer: determination of bulk lifetime and surface recombination velocity. J Appl Phys 61:2282–2293
54. Wang XC, Chen XM, Yang BH (2009) Microstructure and optical properties of polycrystalline ZnO films sputtered under different oxygen flow rates. J Alloys Compd 488:232–237
55. Edwards DF (1998) Silicon. In: Palik ED (ed) Handbook of optical constants of solids. Academic, San Diego, pp 547–569
56. Podolian A, Kozachenko V, Nadtochiy A, Borovoy N, Korotchenkov O (2010) Photovoltage transients at fullerene-metal interfaces. J Appl Phys 107:093706
57. Nadtochiy A, Podolian A, Korotchenkov O, Schmid J, Kancsar E, Schlosser V (2011) Water-based sonochemical cleaning in the manufacturing of high-efficiency photovoltaic silicon wafers. Phys Status Solidi C 8:2927–2930